
Object-Centric Voxelization of Dynamic Scenes via Inverse Neural Rendering

Siyu Gao* **Yanpeng Zhao*** **Yunbo Wang[†]** **Xiaokang Yang**
 MoE Key Lab of Artificial Intelligence, AI Institute, Shanghai Jiao Tong University
 {siyu.gao, zhao-yan-peng, yunbow, xkyang}@sjtu.edu.cn

Abstract

Understanding the compositional dynamics of the world in unsupervised 3D scenarios is challenging. Existing approaches either fail to make effective use of time cues or ignore the multi-view consistency of scene decomposition. In this paper, we propose *DynaVol*, an inverse neural rendering framework that provides a pilot study for learning time-varying volumetric representations for dynamic scenes with multiple entities (like objects). It has two main contributions. First, it maintains a time-dependent 3D grid, which dynamically and flexibly binds the spatial locations to different entities, thus encouraging the separation of information at a representational level. Second, our approach jointly learns grid-level local dynamics, object-level global dynamics, and the compositional neural radiance fields in an end-to-end architecture, thereby enhancing the spatiotemporal consistency of object-centric scene voxelization. We present a two-stage training scheme for *DynaVol* and validate its effectiveness on various benchmarks with multiple objects, diverse dynamics, and real-world shapes and textures. We present visualization at <https://sites.google.com/view/dynavol-visual>.

1 Introduction

Unsupervised learning of the physical world using compositional representations is of fundamental importance for neuro-symbolic AI, which has the great potential to improve the sample efficiency, interpretability, and generalization of learning systems Spelke and Kinzler (2007); Greff et al. (2020). However, it is also challenging due to the unstructured nature of the sensory data. Previous unsupervised approaches for dynamic scene decomposition mainly exploit the temporal cues in consecutive video frames Elsayed et al. (2022); Singh et al. (2022); Kabra et al. (2021), while ignoring the 3D consistency of the object-centric representations, which can be obtained by using a monocular camera moving around the dynamic scene. In this paper, we provide an early study of unsupervised physical scene decomposition and dynamics grounding (in terms of motion segmentation) in 3D scenarios. The core idea is that the object-centric representation needs to meet three conditions:

- (i) It must acquire a comprehensive and abstract notion of the global dynamics of each object, which is essential for maintaining the decoupling of object information.
- (ii) It is required to model the local geometric deformation at the pixel (or voxel) level. More importantly, it needs to be bound to the global object-level representation.
- (iii) It requires the ability to perceive 3D structures, which is challenging when observing a dynamic scene with a monocular camera.

Accordingly, we propose *DynaVol*, an inverse neural rendering framework that learns to perform object-centric voxelization of 3D dynamic scenes. It integrates three network components in a

*Equal contribution.

[†]Corresponding author: Yunbo Wang.

unified differentiable architecture. The first component is a **grid-level local dynamics module** that optimizes the initial volume grid and its spatial transitions to future timestamps in the 4D canonical space Pumarola et al. (2020); Liu et al. (2022). The feature vector at each grid point represents the probability of different objects appearing in its neighborhood. The second component is an **object-level global dynamics module**, which binds the volumetric grid vectors to the representation of global dynamics, and captures the overall motions of individual objects and their interactions using a set of latent features based on the *slot attention* mechanism Locatello et al. (2020); Elsayed et al. (2022). The last component is a **compositional image renderer** that combines the object-centric representation with the neural radiance fields (NeRFs) Mildenhall et al. (2020). It is driven by both the grid-level and object-level representations that change dynamically over time, and provides rich 3D priors by propagating image rendering errors back to the local and global forward modeling processes.

In addition, we present a two-stage training scheme for DynaVol. The first warmup stage provides strong geometric priors to facilitate the decoupling of spatial and temporal features. The second training stage optimizes the entire model on monocular sequential data, so that the initial voxel grid representation can be further refined by fully considering the local and global temporal cues.

We evaluate DynaVol on multiple 3D dynamic scenes with different numbers of objects, diverse motions with different initial velocities, and various shapes and textures. Our approach is shown to outperform the prior art in novel view synthesis. Furthermore, by projecting the object-centric voxel grid representation onto 2D planes, we show that the inverse rendering framework enables fine-grained separation of object-centric information, leading to better performance for object segmentation than the 2D approaches.

The contributions of this paper are summarized as follows:

- We provide an early study of combining object-centric physical inference and dynamic volume rendering, which we call DynaVol. It is a natural solution for unsupervised segmentation through the voxelization of 3D scenes.
- In DynaVol, we introduce a new set of local and global dynamics representations centered on the objects. We bind explicit volume grid vectors to implicit object-level features to maintain representational consistency.
- Through a series of experiments, we empirically verify that the use of inverse rendering techniques is beneficial to the compositional understanding of physical scenes.

2 Related Work

Unsupervised scene decomposition in 2D space. Most existing approaches in this area Greff et al. (2016, 2019); Engelcke et al. (2020); Burgess et al. (2019) use latent features to represent objects in 2D scenarios like CLEVR Johnson et al. (2016). The slot attention method Locatello et al. (2020) extracts object-centric latents through a cross-attention mechanism and repeatedly refines them using GRUs Cho et al. (2014). In the context of video data, SAVi Kipf et al. (2022) extends slot attention into dynamic scenes by updating slots at each frame and uses optical flow data as the reconstruction target. STEVE Singh et al. (2022) improves SAVi by simply replacing the spatial broadcast decoder with an autoregressive Transformer. SAVi++ Elsayed et al. (2022) uses depth information to improve SAVi for modeling static objects with camera motions.

Unsupervised scene decomposition in 3D space. Recent methods Kabra et al. (2021); Chen et al. (2021); Yu et al. (2022); Stelzner et al. (2021); Sajjadi et al. (2022) combine object-centric representations with view-dependent scene modeling techniques like neural radiance fields (NeRFs) Mildenhall et al. (2020). uORF Yu et al. (2022) extracts the background latent and foreground latents from an input static image to handle background and foreground objects separately. ObSuRF Stelzner et al. (2021) adopts the spatial broadcast decoder and takes depth information as training supervision. For dynamic scenes, Li et al. (2022) proposed an auto-encoder framework that incorporates volume rendering to model dynamic scenes. However, it represents the whole scene using a single latent vector (instead of object-centric features), which can be insufficient for complex scenarios with multiple objects and various motions. Guan et al. (2022) proposed to use a set of particle-based explicit representations in the NeRF-based inverse rendering framework, which is particularly designed for fluid physics modeling. Driess et al. (2022) explored the combination of an object-centric

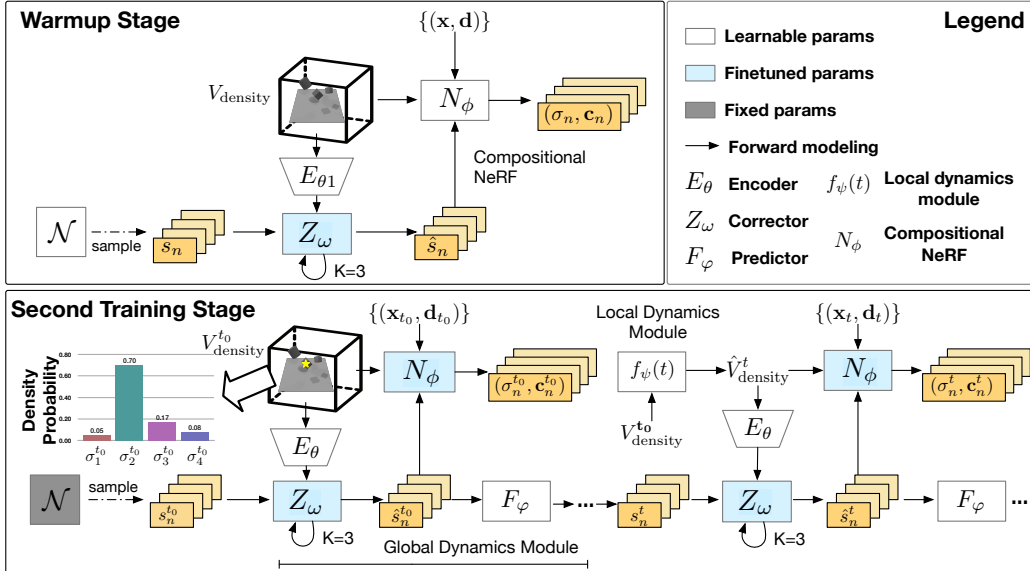


Figure 1: **Top:** In the warmup stage, we train a volume encoder, the slot attention block with a learnable Gaussian distribution, and the compositional NeRF at the initial timestamp. **Bottom:** In the second training stage, we reinitialize the volume encoder, fix the Gaussian priors of slot features, and train the entire DynaVol to render the images collected by a moving monocular camera.

auto-encoder and volume rendering for dynamic scenes, which is the most relevant work to our approach. However, unlike our approach which is totally unsupervised, it requires pre-prepared 2D object segments.

Dynamic scene rendering based on NeRFs. Besides those with object-centric representations, there is another line of work that models 3D dynamics using NeRF-based methods. D-NeRF Pumarola et al. (2020) uses a deformation network to map the coordinates of the dynamic fields to the canonical space. DeVRF Liu et al. (2022) models dynamic scenes with volume grid features Sun et al. (2022) and voxel deformation fields. Recently, D²NeRF Wu et al. (2022) presents a motion decoupling framework. However, unlike DynaVol, it cannot segment multiple moving objects.

3 Method

In this section, we first present the problem setup and overall framework of DynaVol. We then introduce a new set of representations based on object-centric scene voxelization. Next, we discuss the network architecture. Finally, we provide a two-stage training scheme for DynaVol.

3.1 Overview of DynaVol

Problem setup. We assume a sparse set of RGB images of a dynamics scene $\{\mathbf{I}_t^v, \mathbf{T}_t^v\}_{t=1}^T$ collected with a moving monocular camera and corresponding multiple views $\{\mathbf{I}_{t_0}^v, \mathbf{T}_{t_0}^v\}_{v=1}^V$ at the initial timestamp. $\mathbf{I}_t^v \in \mathbb{R}^{H \times W \times 3}$ are images acquired under camera poses $\mathbf{T}_t^v \in \mathbb{R}^{4 \times 4}$, T is the length of video frames, and V is the number of views at the starting moment t_0 . Our model is trained to synthesize $\{\mathbf{I}_t^v\}_{t=1}^T$ and $\{\mathbf{I}_{t_0}^v\}_{v=1}^V$ without further supervision. Formally, the goal is to learn an object-centric projection of $(\mathbf{x}, \mathbf{d}, t) \rightarrow \{(\mathbf{c}_n, \sigma_n)\}_{n=1}^N$, where N is the assumed number of objects and $\mathbf{x} = (x, y, z)$ is a 3D point sampled by the neural renderer, which outputs the density and color for each object at timestamp t and view direction $\mathbf{d} = (\theta_d, \phi_d)$. By re-combining $\{(\mathbf{c}_n, \sigma_n)\}_{n=1}^N$ to approach true pixel values, the model can be forced to learn effective object-centric representations. We evaluate the model for novel view synthesis and scene decomposition tasks.

Overall framework. As shown in Figure 1, DynaVol consists of three modules. It learns the dynamics in a two-stream modeling way, among which, the local dynamics module f_ψ models the

deformation fields at the grid level, starting from a voxel grid V_{density} . The global dynamics module has three sub-modules, including the volume encoder E_θ , the slot attention block Z_ω , and the global dynamics predictor F_φ . It dynamically and flexibly binds the volumetric grid vectors to object-level slot representations and captures the overall motions of individual objects and their interactions using a set of latent features based on slot attention Locatello et al. (2020). Finally, the neural rendering module N_ϕ integrates the above local and global object-centric features in a compositional NeRF. The local grid-level features determine the density weight of each object during color synthesis at each pixel, while the global features serve as inputs for the rendering network to generate object-specific outputs. DynaVol has two training stages, including a static warmup stage and a dynamics learning stage.

What is new in DynaVol? Existing NeRF-based decomposition methods Yu et al. (2022); Stelzner et al. (2021) mainly focus on static scenes, while DynaVol is also designed for object-centric dynamics grounding. Compared with the work from Driess et al. (2022), DynaVol is totally unsupervised and free of 2D masks, *thanks to the novel representation that binds local and global scene properties*.

3.2 Object-Centric Representation

There are two sets of representations in DynaVol, the local grid-level representation based on the 4D volumetric canonical space and the global object-level representation based on the slot attention mechanism, both centered on the objects.

Volumetric representation of object probability. We take inspiration from DVGO Sun et al. (2022) to use a voxel grid to maintain volume density for neural rendering. We extend it with object-centric representations and take a 4D format of V_{density} to represent the density probabilities of different objects. The density probability $\{\sigma_n\}_{n=1}^N$ of any 3D point can be efficiently queried through the trilinear interpolation sampling method:

$$\text{Interp}(\mathbf{x}, V_{\text{density}}) : (\mathbb{R}^3, \mathbb{R}^{N \times N_x \times N_y \times N_z}) \rightarrow \mathbb{R}^N, \quad (1)$$

where N is the assumed number of maximum objects, and (N_x, N_y, N_z) are the resolutions of V_{density} along three axes. We use the softplus activation function after the trilinear interpolation on V_{density} to obtain sharp decision boundaries and precise density values during training.

We discuss the details of the slot representation of global dynamics in the following section. Notably, the most challenging part is to bind the grid-level features and the slot-level features to maintain representational consistency.

3.3 Two-Stream Dynamics Modeling

Local dynamics module. Inspired by D-NeRF Pumarola et al. (2020), the local dynamics module f_ψ learns the deformation field from the voxel grid at the initial timestamp to its canonical space variations at time t . Given any 3D point \mathbf{x} at t , f_ψ predicts a position movement $\Delta\mathbf{x}$ that can be transformed to the scene positions at the first moment by $\mathbf{x} + \Delta\mathbf{x}$. We then query the density probability from $V_{\text{density}}^{t_0}$ by trilinear interpolation:

$$f_\psi(\mathbf{x}, t) = \begin{cases} 0, & \text{for } t = 0, \\ \Delta\mathbf{x}, & \text{for } t \neq 0. \end{cases} \quad (2)$$

Notably, we encode \mathbf{x} , \mathbf{d} , and t into higher dimensions via positional embedding, and f_ψ predicts the object probability grid at an arbitrary time for any 3D point $\forall \mathbf{x}_i \in \{\mathbf{x}\}$:

$$\hat{V}_{\text{density}}^t = \text{Interp}((\mathbf{x}_i + f_\psi(\mathbf{x}_i, t)), V_{\text{density}}^{t_0}). \quad (3)$$

However, f_ψ only focuses on the dynamics in grid neighborhoods. Therefore, we propose the global dynamics module.

Global dynamics module. To extract spacetime properties at a higher representational level, such as the interactions between objects, we adopt the slot attention module Locatello et al. (2020) for the global dynamics module. It infers object-centric latents from the real-time voxel grid V_{density}^t . In other words, our dynamics module is capable of reasoning about the physics of interactions between the objects, which is different from DevRF and D-NeRF trained to memorize the whole scene. We

assume that the latent slot features share the same prior Gaussian distribution with a learnable mean and variance. We sample slots $\mathbf{S}_t \sim \mathcal{N}(\mu, \text{diag}(\sigma)) \in \mathbb{R}^{N \times D}$ for N objects at timestamp $t = t_0$, where D is the dimensionality of each slot. There are three sub-modules that execute in the order given below.

Encoder: At timestamp t , we pass the voxel grid V_{density}^t through a 3D CNN encoder E_θ , which consists of 3 convolutional layers with ReLUs. It outputs a set of flattened features $\mathbf{h}_t \in \mathbb{R}^{M \times D}$, where M is the size of flattened grids and D corresponds to the dimensionality of the slot features.

Corrector: To maintain representational consistency, we refine the slot features by binding them with the grid-level local information. We employ the iterative attention block, denoted by Z_w , to incorporate the local deformation presented by the voxel grid. Specifically, in a single round of slot attention, the slot features interact as follows:

$$\begin{aligned} \mathcal{A}_t &= \text{softmax}_N \left(\frac{1}{\sqrt{D}} k(\mathbf{h}_t) \cdot q(\mathbf{S}_t)^T \right) \in \mathbb{R}^{M \times N}, \\ W_t^{i,j} &= \frac{\mathcal{A}_t^{i,j}}{\sum_{l=1}^M \mathcal{A}_t^{l,j}}, \quad \mathcal{U}_t = W^T \cdot v(\mathbf{h}_t) \in \mathbb{R}^{N \times D}, \end{aligned} \quad (4)$$

where (q, k, v) are learnable linear projections $\mathbb{R}^{D \rightarrow D}$ that map slots dimension to a new dimension space for computing the dot-product similarity Luong et al. (2015), and \sqrt{D} is a fixed softmax temperature Vaswani et al. (2017). Slots features are then updated by a GRU as $\hat{\mathbf{S}}_t = \text{GRU}(\mathcal{U}_t, \mathbf{S}_t)$. We repeat the attention computation and update K times ($K = 3$) and finally obtain the refreshed slot latents $\hat{\mathbf{S}}_t$.

Predictor: To capture the physics of each object and the interactions of multiple objects, we introduce a motion predictor F_φ in forms of the Transformer encoder Vaswani et al. (2017). It predicts \mathbf{S}_{t+1} at the next timestamp:

$$\begin{aligned} \tilde{\mathbf{S}}_t &= \text{LN} \left(\text{MultiHeadAttn}(\hat{\mathbf{S}}_t) + \hat{\mathbf{S}}_t \right), \\ \mathbf{S}_{t+1} &= \text{LN} \left(\text{MLP}(\tilde{\mathbf{S}}_t) + \tilde{\mathbf{S}}_t \right), \end{aligned} \quad (5)$$

where we apply layer normalization (LN) after each residual connection and the multi-head dot-product attention.

Compositional neural renderer. We render the 3D dynamic scene using a compositional NeRF conditioned on object-centric representations, which can be written as $N_\phi(\mathbf{x}, \mathbf{d} \mid \hat{\mathbf{S}})$. Previous compositional NeRF, like uORF Yu et al. (2022), typically uses an MLP to learn a continuous mapping g from sampling point \mathbf{x} , viewing direction \mathbf{d} , and slot features \mathbf{S} , to the emitted densities $\{\sigma_n\}$ and colors $\{\mathbf{c}_n\}$ of different objects. While in our renderer N_ϕ , we only adopt the MLP to learn the object-centric projections g' : $(\mathbf{x}, \mathbf{d}, \hat{\mathbf{S}}) \rightarrow \{\mathbf{c}_n\}$ and query $\{\sigma_n\}$ directly from the voxel grid \hat{V}_{density} at the corresponding timestamp. We here omit the time superscript for simplicity. To compose the predictions of \mathbf{c}_n and σ_n for different objects, we use density-weighted mean to combine all the elements, such that:

$$w_n = \frac{\sigma_n}{\sum_{n=0}^N \sigma_n}, \quad \bar{\sigma} = \sum_{n=0}^N w_n \sigma_n, \quad \bar{\mathbf{c}} = \sum_{n=0}^N w_n \mathbf{c}_n, \quad (6)$$

where $\bar{\sigma}$ and $\bar{\mathbf{c}}$ is the output density and the color of a sampling point. We estimate the color $C(\mathbf{r})$ of a sampling ray with the quadrature rule Max (1995):

$$\hat{C}(\mathbf{r}) = \sum_{i=1}^P T_i (1 - \exp(-\bar{\sigma}_i \delta_i)) \bar{\mathbf{c}}_i, \quad (7)$$

where $T_i = \exp(-\sum_{j=1}^{i-1} \bar{\sigma}_j \delta_j)$, P is the number of sampling points in a certain camera ray, and δ_i is the distance between adjacent samples along the ray.

3.4 Training Procedure

Objectives. Similar to DVGO Sun et al. (2022), at a specific time, we take the rendering loss between the predicted and observed pixel colors, the per-point RGB loss, and the background entropy loss as basic objective terms. The entropy loss can be viewed as a regularization to encourage the renderer to concentrate on either foreground or background:

$$\begin{aligned}\mathcal{L}_{\text{Render}} &= \frac{1}{|\mathcal{R}|} \sum_{r \in \mathcal{R}} \left\| \hat{C}(\mathbf{r}) - C(\mathbf{r}) \right\|_2^2, \\ \mathcal{L}_{\text{Point}} &= \frac{1}{|\mathcal{R}|} \sum_{r \in \mathcal{R}} \left(\frac{1}{P_r} \sum_{i=0}^{P_r} \left\| \bar{\mathbf{c}}_i - C(\mathbf{r}) \right\|_2^2 \right), \\ \mathcal{L}_{\text{Ent}} &= \frac{1}{|\mathcal{R}|} \sum_{r \in \mathcal{R}} -\hat{w}_l^r \log(\hat{w}_l^r) - (1 - \hat{w}_l^r) \log(1 - \hat{w}_l^r),\end{aligned}\quad (8)$$

where \mathcal{R} is the set of sampled rays in a batch, P_r is the number of sampling points along ray r , and \hat{w}_l^r is the color contribution of the last sampling point along r . It is obtained by $\hat{w}_l^r = T_{P_r} (1 - \exp(-\sigma_{P_r} \delta_{P_r}))$.

First training stage: Warmup. Our approach includes two training stages: the static warmup stage and the temporal dynamics grounding stage. The purpose of warmup is to provide valuable 3D geometry information to the next stage and thus reduce the difficulty of dynamics grounding. In this stage, we render multi-view images $\{\mathbf{I}_{t_0}^v\}_{v=1}^V$ of the scene at the first timestamp with the following objectives:

$$\mathcal{L}_{\text{Warmup}} = \mathcal{L}_{\text{Render}} + \alpha_p \mathcal{L}_{\text{Point}} + \alpha_e \mathcal{L}_{\text{Ent}}, \quad (9)$$

where we optimize $V_{\text{density}}^{t_0}$, ω , θ_1 , ϕ , and $\mathcal{N}(\mu, \text{diag}(\sigma))$. We adopt the empirical values of the hyperparameters from previous literature Liu et al. (2022). $\mathcal{L}_{\text{Warmup}}$ encourages the model to learn the geometric 3D priors. Note that, as shown in Figure 1, $V_{\text{density}}^{t_0}$ is trained in the warmup stage. In this stage, we perform an operation based on the “connected components” to initialize the 4D density voxel grid with N object channels. Concretely, we use the density values after softplus and filter the invalid locations with density values lower than a pre-defined threshold. We assume that for a particular object, its density should be in the same connected component; while for objects at different spatial locations, their densities should be in different connected components. Preliminary experiments show that this method can effectively improve the final performance in the next training stage.

Second training stage: Dynamics grounding. In the second stage, we load $V_{\text{density}}^{t_0}$, ω , ϕ , and $\mathcal{N}(\mu, \text{diag}(\sigma))$ from the warmup stage, which can introduce rich priors for the efficient learning of local and global object-centric dynamics. Since the number of slots in the two stages remains different, we do not load the parameters θ_1 but re-initialize the volume encoder. We take T consecutive images $\{\mathbf{I}_t^v\}_{t=1}^T$ uniformly collected by a monocular in one second. Each image is taken from a random viewpoint. The benefit of optimizing the entire model on monocular sequential data is that it can further refine the initial voxel grid representation $V_{\text{density}}^{t_0}$ using the temporal cues of local and global dynamics. To maintain the 3D prior knowledge of the initial scene, we include $\mathcal{L}_{\text{Warmup}}$ at the first timestamp in the overall loss \mathcal{L}_{Dyn} for the second training stage. Finally, we have:

$$\mathcal{L}_{\text{Dyn}} = \sum_{t=1}^T (\mathcal{L}_{\text{Render}} + \alpha_p \mathcal{L}_{\text{Point}} + \alpha_e \mathcal{L}_{\text{Ent}}) + \alpha_w \mathcal{L}_{\text{Warmup}}, \quad (10)$$

where we fix $\mathcal{N}(\mu, \text{diag}(\sigma))$, finetune $(V_{\text{density}}^{t_0}, \omega, \phi)$ from the warmup stage, and train (θ, φ, ψ) from scratch. We set the same value of α_p and α_e as in the first stage and tune α_w on different datasets.

4 Experiments

4.1 Implementation Details

We set the size of the voxel grid to 110^3 and the dimension of slot features to 64. We use 8 hidden layers with 256 channels in the renderer. We use the Adam optimizer with a batch of 4,096 rays in the

Table 1: Novel view synthesis results of our approach compared with D-NeRF Pumarola et al. (2020) and DeVRF Liu et al. (2022), as well as their variants for dynamic scenes (see text for details). We evaluate the results averaged over 60 novel views per timestamp.

METHOD	3OBJFALL		3OBJRAND		3OBJMETAL		3FALL+3STILL	
	PSNR↑	SSIM↑	PSNR↑	SSIM↑	PSNR↑	SSIM↑	PSNR↑	SSIM↑
D-NeRF	28.54	0.946	12.62	0.853	27.83	0.945	24.56	0.908
D-NeRF-2STG	30.00	0.957	26.33	0.931	26.70	0.911	22.40	0.883
DeVRF	24.92	0.927	22.27	0.912	25.24	0.931	24.80	0.931
DeVRF-DYN	21.15	0.872	19.50	0.865	21.20	0.876	20.51	0.859
DynaVol	32.08	0.964	29.85	0.959	29.76	0.954	29.45	0.951

METHOD	6OBJFALL		8OBJFALL		3OBJREALSIMP		3OBJREALCMPX	
	PSNR↑	SSIM↑	PSNR↑	SSIM↑	PSNR↑	SSIM↑	PSNR↑	SSIM↑
D-NeRF	28.27	0.940	27.44	0.923	27.04	0.927	20.73	0.864
D-NeRF-2STG	26.96	0.925	26.35	0.909	27.45	0.935	20.95	0.857
DeVRF	24.83	0.905	24.87	0.915	24.81	0.922	21.77	0.891
DeVRF-DYN	19.89	0.836	20.08	0.835	20.67	0.859	18.44	0.822
DynaVol	32.00	0.962	30.66	0.951	29.59	0.949	25.91	0.905

Table 2: Comparisons with existing approaches based on 2D/3D object-centric representations, *i.e.*, SAVi Elsayed et al. (2022) and uORF Yu et al. (2022). For uORF, we present novel view synthesis and object segmentation results. For SAVi, since it requires videos with fixed viewpoints, we generate different image sequences at 4 fixed camera positions and present the average results of SAVi on these videos. To compare with it, we test DynaVol (FixCam) with images that are also collected at these fixed camera views.

METHOD	3OBJRAND			6OBJFALL			8OBJFALL		
	PSNR↑	SSIM↑	FG-ARI↑	PSNR↑	SSIM↑	FG-ARI↑	PSNR↑	SSIM↑	FG-ARI↑
SAVi	—	—	4.21	—	—	7.46	—	—	7.44
DynaVol (FixCam)	30.68	0.955	85.21	32.38	0.956	92.86	31.52	0.950	95.97
uORF	6.65	0.556	38.65	6.63	0.50	29.23	6.89	0.529	31.93
DynaVol	29.85	0.959	91.01	32.00	0.962	95.71	30.66	0.951	94.53

first stage and 1,024 rays in the second stage. The base learning rates are 0.1 for the voxel grid and $1e^{-3}$ for all model parameters in the warmup stage and then adjusted to 0.05 and $5e^{-4}$ in the second stage. The two training stages last for 20k and 50k iterations respectively. The hyperparameters in the loss functions are set to $\alpha_p = 0.1$, $\alpha_e = 0.01$, $\alpha_w = 1.0$ if not stated otherwise. Since previous slot attention-based methods typically employ large-scale training scenes, for a fair comparison, we load the parameters of Z_ω (to be finetuned in the first stage) and F_φ (to be finetuned in the second stage) from a pretrained SAVi Kipf et al. (2022) on the MOVi-A dataset. All experiments run on a single RTX3090 GPU.

4.2 Experimental Setup

We evaluate DynaVol on both scene representation (via scene segmentation) and novel view synthesis in the following eight scenes. For each scene, we capture V -view ($V = 60$) static images of the initial scene and a dynamic sequence with $T = 60$ timestamps which is rendered from viewpoints randomly sampled at different moments from the upper hemisphere as training data and randomly select another different view at each timestamp for the test, all in 512×512 pixels.

Dataset. We build 8 synthetic dynamic scenes using Kubric Greff et al. (2022) with different numbers of objects (in different colors and shapes), diverse motions with different initial velocities, different materials, and real-world shapes and textures.

- **3ObjFall.** This scene is a simple scene that consists of three geometrically shaped objects with different colors, each with a random initial position, followed by a free-fall motion along the Z-axis.
- **3ObjRand.** Based on *3ObjFall*, we add random initial velocities for each object.

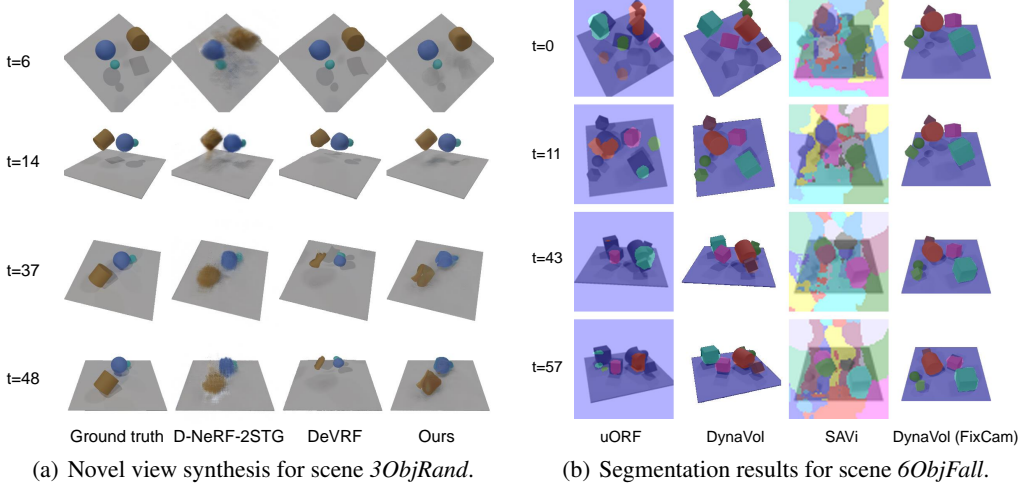
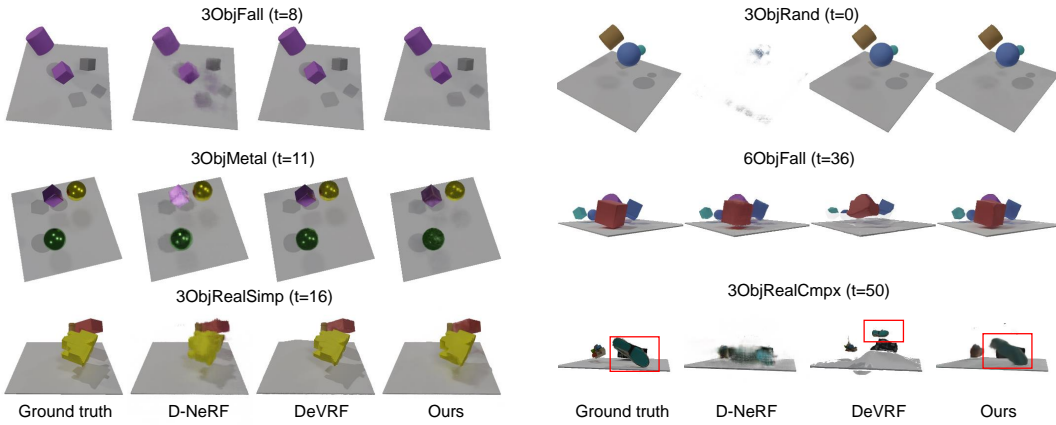


Figure 2: Visualization of novel view synthesis and segmentation at different timestamps.



- **3ObjMetal.** Based on the *3ObjFall* scene, we replace the object material from “Rubber” to “Metal”.
- **3Fall+3Still.** Based on the *3ObjFall* scene, we add another three static objects and improve the complexity of the object geometry and color.
- **6ObjFall & 8ObjFall.** Based on the *3ObjFall* scene, we increase the number of objects to 6 and 8.
- **3ObjRealSimp.** We replace the objects in *3ObjFall* with real-world objects with simple textures.
- **3ObjRealCmpx.** We replace the objects in *3ObjFall* with real-world objects with complex textures.

Metrics. For quantitative comparison of the novel view synthesis problem, we report Mean Squared Error (MSE), Peak Signal-to-Noise Ratio (PSNR), and Structural Similarity (SSIM) Wang et al. (2004). Additionally, to evaluate segmentation quality in a way that is compatible with 2D methods, we use Foreground Adjusted Rand Index (FG-ARI) as our metric, which measures clustering similarity according to the ground truth foreground objects mask where a random segmentation would score 0 and a perfect segmentation would score 1.

Compared methods. We compare DynaVol with various benchmarks, including 3D scene modeling methods D-NeRF, DeVRF, 2D image segmentation methods SAVi, and 3D object-centric methods uORF. Since our method is first trained on static data, for a fair comparison, we also implement a

Table 3: Ablation study on the impact of the *warmup* loss. We show novel view synthesis results averaged over all dynamic scenes.

METHOD	PSNR↑	SSIM↑
DYNAVOL w/o $\mathcal{L}_{\text{WARMUP}}$	28.16	0.939
DYNAVOL	29.56	0.947

Table 4: Ablation study on the impact of the $\mathcal{L}_{\text{Point}}$ loss. We show novel view synthesis and object segmentation results on three datasets.

α_p	3OBJFALL			6OBJFALL			3OBJREALSIMP		
	PSNR↑	SSIM↑	ARI-FG↑	PSNR↑	SSIM↑	ARI-FG↑	PSNR↑	SSIM↑	ARI-FG↑
0.0	30.83	0.956	68.21	31.36	0.959	95.21	28.40	0.937	55.18
0.1(OURS)	32.08	0.964	97.08	32.00	0.962	95.71	29.59	0.949	85.17
1.0	21.28	0.852	20.95	26.69	0.928	90.86	26.30	0.928	80.71

2-stage D-NeRF which is first trained on static data and then moves to the dynamic sequence. Besides, since DeVRF is trained on a 4-view dynamic sequence, we additionally trained DeVRF with the same data as ours, *i.e.*, viewpoints are randomly sampled from the upper hemisphere. Both two variants of DeVRF are trained without the optical flow loss proposed in the paper. For SAVi and uORF, we use the models pretrained on MOVi-A and CLEVR567, respectively, which are similar to our scenes. We try to finetune them on our dataset, however, it does not improve the model performance significantly.

4.3 Novel View Synthesis Results for Dynamic Scenes

We evaluate the performance of DynaVol on the novel view synthesis task with other two 3D benchmarks (D-NeRF, DeVRF) and its variants (2-stage version for D-NeRF is labeled as D-NeRF-2Stg, DeVRF trained on the same data as ours is labeled as DEVRF-Dyn). As shown in Table 1, DynaVol achieves the best performance in terms of PSNR, SSIM, and MSE in **all** datasets. Notably, DynaVol outperforms the second-best method by a large margin even in those difficult scenes (*i.e.*, 6ObjFall, 3Fall+3Still, and 3ObjRealCmpx) with 16.99% increment in PSNR, 2.02% increment in SSIM and 43.35% decrement in MSE on average. There is no significant difference between D-NeRF and D-NeRF-2Stg in most scenes except for 3ObjRand (D-NeRF fails to model 3ObjRand as shown in Figure 3), which illustrates the effectiveness of our two-stage training scheme. Besides, DeVRF-Dyn has an apparent performance degradation compared to the standard version due to it is not specifically designed for the dynamic dataset collected by a monocular.

Figure 3 demonstrates qualitative comparisons with other methods and it shows that DynaVol can capture the 3D appearance of different objects and the corresponding motion patterns at an arbitrary timestamp and render a competitive result in a novel view. By contrast, D-NeRF fails to model complex motion patterns (see 3ObjRand) and performs poorly on the appearance modeling of different objects when facing complex textures (see 3ObjRealCmpx and 3ObjRealSimp).

Figure 2(a) shows a more specific novel view synthetic results on 3ObjRand scene with timestamps on $t = 6$, $t = 14$, $t = 37$, and $t = 48$ respectively. Considering the synthetic results of D-NeRF on this dataset in Figure 3, we choose its variant as an alternative. It can be found that D-NeRF-2Stg produces blurry in all sampled timestamps and DeVRF suffers from severe deformation and position shift in $t = 37$ and $t = 48$, while DynaVol renders relatively clearer and more precise images.

4.4 Unsupervised Object Segmentation Results

To get the 2D segmentation results, we assign the rays to different slots according to the contribution of each slot to the final color of the ray. Suppose σ_{in} is the density of slot n at point i , we can get $w_{in} = \sigma_{in}/\sum_{n=0}^N \sigma_{in}$ and $\beta_n = \sum_{i=1}^P T_i(1 - \exp(-\sigma_i \delta_i))w_{in}$ respectively, where w_{in} is the corresponding density probability and β_n is the color contribution to the final color of slot n . Then we can get the predicted label by $\hat{y}(\mathbf{r}) = \text{argmax}_n(\beta_n)$.

Table 5: Ablation study on the impact of the first training stage. We show novel view synthesis and segmentation results on the 3ObjFall scene.

METHOD (DYNAVOL)	PSNR↑	SSIM↑	ARI-FG↑
W/O WARM-UP STAGE	30.87	0.962	94.45
W/ WARM-UP STAGE	32.08	0.964	97.08

Table 6: Ablation study on the necessity of the 4D volumetric representation V_{density} . We show novel view synthesis and object segmentation results on the 3ObjFall and 3ObjRealSimp datasets.

METHOD	3OBJFALL			3OBJREALSIMP		
	PSNR↑	SSIM↑	ARI-FG↑	PSNR↑	SSIM↑	ARI-FG↑
BASELINE-A	27.77	0.922	32.86	28.06	0.934	3.25
BASELINE-B	24.63	0.915	61.96	25.85	0.892	53.59
BASELINE-C	20.94	0.865	37.32	21.65	0.878	43.64
DYNAVOL	32.08	0.964	97.09	29.59	0.949	85.17

In Table 2 we compare our method with the other two segmentation benchmarks. Since SAVi is a 2D segmentation method that only works on the dynamic scene with a fixed camera position, we evaluate its average performance of metrics FG-ARI with DynaVol (labeled as DynaVol(FixCam)) on four fixed one-view dynamic sequences with distinct positions. As for uORF, it mainly focuses on static scenes, so we process the dynamic sequence into T static single scenes as its inputs and evaluate its average performance on the whole sequence. Results show that our method significantly outperforms all approaches, both in reconstruction quality and segmentation results. It is worth mentioning that we take ARI-FG as the segmentation metrics. The higher the ARI-FG, the method has better segmentation results and temporal consistency.

Figure 2(b) shows the results of the qualitative comparison. DynaVol handles well on object occlusion and ensures object-slot correspondence consistency both in 3D and temporal aspects across multiple views (*i.e.* object always has a fixed color). While SAVi underperforms in this scene and uORF lacks consistency along the time, *i.e.*, the same object is assigned to different slots at different timestamps.

4.5 Ablation Studies

Analyses of loss functions. In Table 3, we evaluate the impact of $\mathcal{L}_{\text{Warmup}}$ in the second training phase of DynaVol. It shows that DynaVol has better performance with $\mathcal{L}_{\text{Warmup}}$, indicating that the 3D priors are still essential for the dynamics grounding training stage. While in Table 4, we explore the effectiveness of $\mathcal{L}_{\text{point}}$ in both of the training phases by setting the weight (α_p) of per-point RGB loss as $\alpha_p = 0.0$, $\alpha_p = 0.1$ (DynaVol’s setting) and $\alpha_p = 1.0$. It can be found that $\alpha_p = 0.1$ performs better than $\alpha_p = 0.0$, indicating that a conservative use of $\mathcal{L}_{\text{point}}$ can improve the performance. A possible reason is that it eases the training process by moderately penalizing the discrepancy of nearby sampling points on the same ray. When the weight of $\mathcal{L}_{\text{point}}$ increases to $\alpha_p = 1.0$, the performance of the method decreases significantly. It shows that a strong $\mathcal{L}_{\text{point}}$ may introduce bias to neural rendering and affect the final results.

Analyses of the warmup stage. We conduct another set of ablation studies by removing the first training stage on the 3ObjFall scene. The results are shown in Table 5, where we can see a significant drop in all three metrics. This illustrates that DynaVol learns valuable 3D geometry biases which reduce the difficulty of dynamics grounding.

Analyses of the volumetric representation. Unlike in DVGO, the volumetric representation V_{density} in DynaVol explicitly represents the probability that each object is present there. To evaluate the necessity of this kind of representation, we add three additional baseline models on the 3ObjFall and 3ObjRealSimp scenes, which has the below definition. **Baseline-A:** We discard V_{density} and the 3D volume encoder E_θ , and then use the 2D image encoder in SAVi instead to compute the slot features based on image inputs of training views. After that we use the renderer to predict both the object-specific color and density values (\mathbf{c}_n, σ_n), while in DynaVol, we take σ_n from V_{density} . **Baseline-B:** We discard the 3D volume encoder, and instead use the 2D image encoder in SAVi to

Table 7: Ablation study on the impact of slot attention. We show novel view synthesis and segmentation results on the 6ObjFall and 3ObjRealSimp scenes.

METHOD	6OBJFALL			3OBJREALSIMP		
	PSNR↑	SSIM↑	ARI-FG↑	PSNR↑	SSIM↑	ARI-FG↑
w/o SLOTATTN	30.13	0.954	89.37	25.02	0.912	65.22
DYNAVOL	32.00	0.962	95.71	29.59	0.949	85.17

Table 8: Ablation study on the impact of two dynamics modules. We show novel view synthesis and segmentation results on the 6ObjFall scene.

METHOD	PSNR↑	SSIM↑	ARI-FG↑
w/o GLOBAL-SLOT-FEAT	19.17	0.776	42.96
w/o LOCAL-DYN-MODULE	21.49	0.870	47.98
DYNAVOL(FULL)	32.00	0.962	95.71

compute the slot features based on image inputs of training views. Then we keep V_{density} and make the renderer unchanged. **Baseline-C**: We use the same 2D image decoder as SAVi, and add an image reconstruction loss between the input image and output of the 2D decoder. While other parts keep the same as Baseline-B. Results can be seen from Table 6, which shows that the volumetric feature grid V_{density} and the 3D volume encoder E_θ are effective for both rendering and unsupervised segmentation of dynamic scenes.

Analyses of the slot attention module. We conduct an ablation study of discarding the slot attention module on the 6ObjFall and 3ObjRealSimp datasets. The results in Table 7 show that without a slot attention module, the performance decreases slightly. The use of slot attention in DynaVol plays an important role in two ways. Firstly, it aggregates information from the grid-level object probabilities in V_{density} , and associates the local representation (h_t) with the global features of object-level dynamics (S_t). Secondly, it exploits the multi-head attention mechanism to map the slot features of different objects to different subspaces, thereby preventing them from collapsing to similar representations.

Analyses of two dynamics modules. We conduct an ablation study to evaluate the necessity of two dynamics modules on the 6ObjFall by discarding the global slot features and the local dynamics module respectively. From Table 8, it can be seen that the absence of either part of the two dynamic modules will cause significant performance degradation.

5 Conclusion

In this paper, we presented an early study of object-centric dynamics understanding in 3D scenarios. In contrast, none of the existing approaches for unsupervised scene decomposition can satisfy the spatiotemporal consistency of the learned object representations. We proposed DynaVol, a compositional neural rendering framework based on object-centric volumetric features. It has two technical contributions. First, it provides a new time-varying 3D representation of the dynamic scenes based on the 4D canonical space, which represents the binding probability of each grid location to a symbol-like entity such as an object. Second, we combined grid-level local dynamics modeling, object-level global dynamics modeling, and compositional neural rendering in an end-to-end architecture, so as to enhance the spatiotemporal consistency of the learned object-centric voxelization. Furthermore, we presented a two-stage training scheme and validated the effectiveness of DynaVol in a wide variety of dynamic scenes with multiple objects, different dynamics, and real-world shapes and textures.

An unsolved problem is that, like the existing inverse rendering method for static scene decomposition Yu et al. (2022), DynaVol still requires multi-view images in the warmup stage. A potential solution in the future is to design a more effective training scheme to decouple the 3D geometric representations and the temporal deformations. This problem does not affect the fairness of experimental comparisons.

Acknowledgement

This work was supported by NSFC (62250062, U19B2035, 62106144), Shanghai Municipal Science and Technology Major Project (2021SHZDZX0102), the Fundamental Research Funds for the Central Universities, and Shanghai Sailing Program (21Z510202133).

References

Elizabeth S Spelke and Katherine D Kinzler. Core knowledge. *Developmental science*, 2007.

Klaus Greff, Sjoerd Van Steenkiste, and Jürgen Schmidhuber. On the binding problem in artificial neural networks. *arXiv preprint arXiv:2012.05208*, 2020.

Gamaleldin F. Elsayed, Aravindh Mahendran, Sjoerd van Steenkiste, Klaus Greff, Michael Curtis Mozer, and Thomas Kipf. SAVi++: Towards end-to-end object-centric learning from real-world videos. In *NeurIPS*, 2022.

Gautam Singh, Yi-Fu Wu, and Sungjin Ahn. Simple unsupervised object-centric learning for complex and naturalistic videos. In *NeurIPS*, 2022.

Rishabh Kabra, Daniel Zoran, Goker Erdogan, Loic Matthey, Antonia Creswell, Matt Botvinick, Alexander Lerchner, and Chris Burgess. SIMONe: View-invariant, temporally-abstracted object representations via unsupervised video decomposition. In *NeurIPS*, 2021.

Albert Pumarola, Enric Corona, Gerard Pons-Moll, and Francesc Moreno-Noguer. D-NeRF: Neural radiance fields for dynamic scenes. In *CVPR*, 2020.

Jia-Wei Liu, Yan-Pei Cao, Weijia Mao, Wenqiao Zhang, David Junhao Zhang, Jussi Kepo, Ying Shan, Xiaohu Qie, and Mike Zheng Shou. DeVRF: Fast deformable voxel radiance fields for dynamic scenes. In *NeurIPS*, 2022.

Francesco Locatello, Dirk Weissenborn, Thomas Unterthiner, Aravindh Mahendran, Georg Heigold, Jakob Uszkoreit, Alexey Dosovitskiy, and Thomas Kipf. Object-centric learning with slot attention. In *NeurIPS*, 2020.

Ben Mildenhall, Pratul P Srinivasan, Matthew Tancik, Jonathan T Barron, Ravi Ramamoorthi, and Ren Ng. Nerf: Representing scenes as neural radiance fields for view synthesis. In *ECCV*, 2020.

Klaus Greff, Antti Rasmus, Mathias Berglund, Tele Hao, Harri Valpola, and Jürgen Schmidhuber. Tagger: Deep unsupervised perceptual grouping. In *NeurIPS*, 2016.

Klaus Greff, Raphaël Lopez Kaufman, Rishabh Kabra, Nick Watters, Christopher Burgess, Daniel Zoran, Loic Matthey, Matthew Botvinick, and Alexander Lerchner. Multi-object representation learning with iterative variational inference. In *ICML*, 2019.

Martin Engelcke, Adam R Kosiorek, Oiwi Parker Jones, and Ingmar Posner. Genesis: Generative scene inference and sampling with object-centric latent representations. In *ICLR*, 2020.

Christopher P Burgess, Loic Matthey, Nicholas Watters, Rishabh Kabra, Irina Higgins, Matt Botvinick, and Alexander Lerchner. Monet: Unsupervised scene decomposition and representation. In *CVPR*, 2019.

Justin Johnson, Bharath Hariharan, Laurens van der Maaten, Li Fei-Fei, C. Lawrence Zitnick, and Ross B. Girshick. CLEVR: A diagnostic dataset for compositional language and elementary visual reasoning. In *CVPR*, 2016.

Kyunghyun Cho, Bart van Merriënboer, Çağlar Gülcehre, Dzmitry Bahdanau, Fethi Bougares, Holger Schwenk, and Yoshua Bengio. Learning phrase representations using RNN encoder–decoder for statistical machine translation. In *EMNLP*, 2014.

Thomas Kipf, Gamaleldin F Elsayed, Aravindh Mahendran, Austin Stone, Sara Sabour, Georg Heigold, Rico Jonschkowski, Alexey Dosovitskiy, and Klaus Greff. Conditional object-centric learning from video. In *ICLR*, 2022.

Chang Chen, Fei Deng, and Sungjin Ahn. ROOTS: Object-centric representation and rendering of 3D scenes. *Journal of Machine Learning Research*, 2021.

Hong-Xing Yu, Leonidas J Guibas, and Jiajun Wu. Unsupervised discovery of object radiance fields. In *ICLR*, 2022.

Karl Stelzner, Kristian Kersting, and Adam R Kosiorek. Decomposing 3D scenes into objects via unsupervised volume segmentation. *arXiv preprint arXiv:2104.01148*, 2021.

Mehdi SM Sajjadi, Daniel Duckworth, Aravindh Mahendran, Sjoerd van Steenkiste, Filip Pavetić, Mario Lučić, Leonidas J Guibas, Klaus Greff, and Thomas Kipf. Object scene representation transformer. In *NeurIPS*, 2022.

Yunzhu Li, Shuang Li, Vincent Sitzmann, Pulkit Agrawal, and Antonio Torralba. 3D neural scene representations for visuomotor control. In *CoRL*, 2022.

Shanyan Guan, Huayu Deng, Yunbo Wang, and Xiaokang Yang. NeuroFluid: Fluid dynamics grounding with particle-driven neural radiance fields. In *ICML*, 2022.

Danny Driess, Zhiao Huang, Yunzhu Li, Russ Tedrake, and Marc Toussaint. Learning multi-object dynamics with compositional neural radiance fields. *arXiv preprint arXiv:2202.11855*, 2022.

Cheng Sun, Min Sun, and Hwann-Tzong Chen. Direct voxel grid optimization: Super-fast convergence for radiance fields reconstruction. In *CVPR*, 2022.

Tianhao Wu, Fangcheng Zhong, Andrea Tagliasacchi, Forrester Cole, and Cengiz Özti̇reli. D2NeRF: Self-supervised decoupling of dynamic and static objects from a monocular video. In *NeurIPS*, 2022.

Minh-Thang Luong, Hieu Pham, and Christopher D Manning. Effective approaches to attention-based neural machine translation. *arXiv preprint arXiv:1508.04025*, 2015.

Ashish Vaswani, Noam Shazeer, Niki Parmar, Jakob Uszkoreit, Llion Jones, Aidan N Gomez, Łukasz Kaiser, and Illia Polosukhin. Attention is all you need. In *NeurIPS*, 2017.

Nelson Max. Optical models for direct volume rendering. *IEEE Transactions on Visualization and Computer Graphics*, 1995.

Klaus Greff, Francois Belletti, Lucas Beyer, Carl Doersch, Yilun Du, Daniel Duckworth, David J. Fleet, Dan Gnanapragasam, Florian Golemo, Charles Herrmann, Thomas Kipf, Abhijit Kundu, Dmitry Lagun, Issam H. Laradji, Hsueh-Ti Liu, Henning Meyer, Yishu Miao, Derek Nowrouzezahrai, Cengiz Özti̇reli, Etienne Pot, Noha Radwan, Daniel Rebain, Sara Sabour, Mehdi S. M. Sajjadi, Matan Sela, Vincent Sitzmann, Austin Stone, Deqing Sun, Suhani Vora, Ziyu Wang, Tianhao Wu, Kwang Moo Yi, Fangcheng Zhong, and Andrea Tagliasacchi. Kubric: A scalable dataset generator. In *CVPR*, 2022.

Zhou Wang, Alan Conrad Bovik, Hamid R. Sheikh, and Eero P. Simoncelli. Image quality assessment: from error visibility to structural similarity. *IEEE Transactions on Image Processing*, 2004.